

## Article

# Improving Welding Penetration and Mechanical Properties via Activated-Flux Smearing by Tungsten Inert Gas Arc Welding

Shiqi Yue<sup>1,2</sup>, Yong Huang<sup>1,2,\*</sup> , Xiaoquan Yu<sup>3</sup>, Jia Zhang<sup>1,2</sup>, Yu Ni<sup>1,2</sup> and Ding Fan<sup>1,2</sup> 

<sup>1</sup> School of Materials Science and Engineering, Lanzhou University of Technology, Lanzhou 730050, China; 19119376167@163.com (S.Y.); 17794432149@163.com (J.Z.); niyu2008@163.com (Y.N.); fand@lut.edu.cn (D.F.)

<sup>2</sup> State Key Laboratory of Advanced Processing and Recycling of Non-Ferrous Metal, Lanzhou 730050, China

<sup>3</sup> Taizhou Institute of Zhejiang University, Zhejiang University, Taizhou 318000, China; yuxiaoquangood@163.com

\* Correspondence: hyorhot@lut.edu.cn

**Abstract:** For the welding process of thick-walled structural components in liquid rocket engines, the activated-flux TIG method can effectively address issues such as the formation of intermetallic phases in the weld seams, thereby enhancing mechanical performance. The present study investigates the activated-flux TIG welding technique on 10mm thick 1Cr21Ni5Ti duplex stainless steel plates. Various activated-flux, including  $\text{-SiO}_2$ ,  $\text{TiO}_2$ ,  $\text{V}_2\text{O}_5$ ,  $\text{NiO}$ ,  $\text{MnO}_2$ ,  $\text{CaO}$ ,  $\text{AlCl}_3$ ,  $\text{CaF}_2$ ,  $\text{B}_2\text{O}_3$ ,  $\text{Cr}_2\text{O}_3$ , and  $\text{Al}_2\text{O}_3$ , were examined to understand their impact on the weld-bead geometry. The aim was to determine the optimal activator ratio for the effective welding of 1Cr21Ni5Ti duplex stainless steel. The weld-shift experiment confirmed that the deep penetration observed in flux-assisted welding is attributed to Marangoni convection in the molten pool. Comprehensive evaluations and analyses were performed on the microstructure and mechanical properties of the normal welded joint and the A-TIG welded joint. Finally, the study delves into a discussion on the factors influencing changes in the weld penetration, microstructure, and mechanical properties of the weld.

**Keywords:** 1Cr21Ni5Ti steel; A-TIG; Marangoni convection; weld formation



**Citation:** Yue, S.; Huang, Y.; Yu, X.; Zhang, J.; Ni, Y.; Fan, D. Improving Welding Penetration and Mechanical Properties via Activated-Flux Smearing by Tungsten Inert Gas Arc Welding. *Metals* **2023**, *13*, 2017. <https://doi.org/10.3390/met13122017>

Academic Editors: Jean-Michel Bergheau and Frank Czerwinski

Received: 10 November 2023

Revised: 2 December 2023

Accepted: 13 December 2023

Published: 15 December 2023



**Copyright:** © 2023 by the authors. Licensee MDPI, Basel, Switzerland. This article is an open access article distributed under the terms and conditions of the Creative Commons Attribution (CC BY) license (<https://creativecommons.org/licenses/by/4.0/>).

## 1. Introduction

Liquid rocket engines are the key power equipment in the field of modern space exploration and national defense, and their performance and reliability directly affect the performance of launch vehicles. As the cornerstone of aviation development, the reliability of liquid rocket engines has become an indispensable research topic. Duplex stainless steel is known for its oxidation resistance, acid corrosion resistance, high level of toughness and excellent weld ability [1–5], and it is widely used in the manufacture of key structural components of liquid rocket engine combustion chambers. The performance of its welded joints has become a key factor affecting its reliability. Various welding techniques are employed for 1Cr21Ni5Ti duplex stainless steel, including bounding welding (BW), laser-beam welding (LBW), hot isostatic pressing (HIP), and friction-stir welding (FSW). However, when using these methods to weld thick-walled components, challenges like porosity, undercuts, compromised toughness, and the formation of intermetallic phases can pose significant concerns [6–9].

Tungsten inert gas (TIG) welding, as a conventional welding method, is widely adopted in various metal-processing fields. However, conventional TIG welding faces some shortcomings, such as low production efficiency and the need for a groove to increase weld penetration in the welding of thick plates [10,11]. As the heat input during welding increases, it leads to abnormal grain growth within the weld. Additionally, a substantial amount of ferrite is generated, diminishing the microstructure and properties of the weld [4,12–15]. Hence, activated-flux TIG welding (A-TIG) has emerged as a primary welding process for thick-walled structural parts made of 1Cr21Ni5Ti duplex stainless

steel. A-TIG offers advantages such as cost-effectiveness, a notable increase in single-pass melt depth, and minimal alterations in performance [16–18]. Activated-flux TIG welding involves applying an activating agent to the workpiece’s surface before initiating TIG welding, allowing the preservation of TIG characteristics while notably enhancing the weld depth and mechanical properties. During welding, the inclusion of alloying elements and adjustments in the heat input influence the ferrite and austenite phase content within the weld. Achieving an appropriate ferrite-to-austenite phase ratio is a crucial determinant of the welded joint’s mechanical properties [10,19–21]. In the context of stainless-steel thick-walled structural components, A-TIG welding primarily counters the Marangoni convection within the molten pool, significantly augmenting weld penetration and thereby reducing the width of the heat-affected zone [22–24]. Simultaneously, mechanical properties like tensile strength and hardness exhibit minimal alterations [25,26].

In this investigation, the reversal of Marangoni convection was observed in situ by a high-speed camera. To investigate the primary cause of the increased penetration depth, we devised an experimental design involving a weld shift. Furthermore, we analyzed the factors contributing to the reduced mechanical properties of the weld by studying the pole diagram, the phase diagram, and the composition of second-phase particle elements in the weld microstructure. The activated-flux TIG welding of 1Cr21Ni5Ti duplex stainless steel was studied. The impact of various activated-flux on the weld-bead geometry and penetration was examined. Subsequently, the microstructure and mechanical properties of the base material, the TIG-welded joint, and the A-TIG-welded joint were evaluated and analyzed. The reasons behind the alterations in weld penetration, microstructure, and mechanical properties resulting from the application of an activated-flux during TIG welding were discussed.

## 2. Experimental Details

### 2.1. Materials

The chemical composition of the 1Cr21Ni5Ti duplex stainless steel is presented in Table 1. For the A-TIG butt-welding experiment, we utilized a specimen of 1Cr21Ni5Ti duplex stainless steel with size of 100 mm × 50 mm × 10 mm. Figure 1 shows the activated-flux TIG welding process, and the corresponding welding process parameters are listed in Table 2.

**Table 1.** Chemical composition of the 1Cr21Ni5Ti duplex stainless steel (Wt.%).

Elements	Si	Mn	Cr	Ni	Ti	C	Al	Fe
Content	0.49	0.58	20.42	5.26	0.55	0.12	0.09	Bal.

**Table 2.** Basic process parameters.

Welding Current I/A	Welding Speed V/(mm/s)	Shielding Gas Flow Rate Q (L/min)	Arc Length L/mm	Type of Active Agent
260	1.76	15	3	0.033NiO + 0.632SiO <sub>2</sub> + 0.037TiO <sub>2</sub> + 0.162Cr <sub>2</sub> O <sub>3</sub> + 0.137Al <sub>2</sub> O <sub>3</sub>

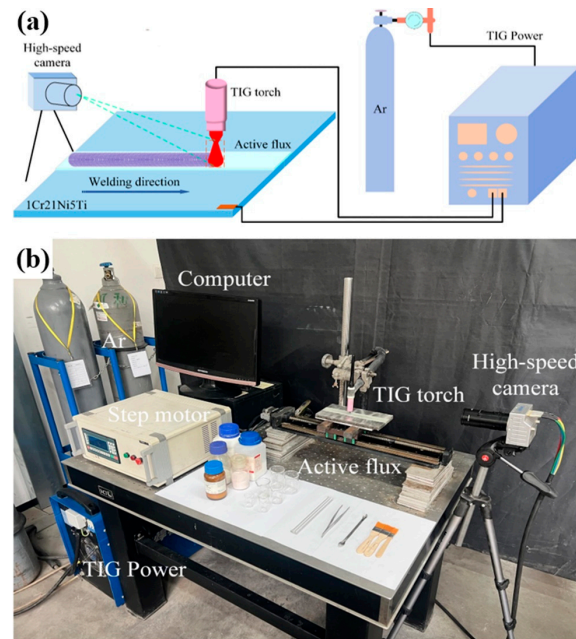


**Figure 1.** Activated-flux TIG welding: (a) Schematic diagram; (b) Profile display.

## 2.2. Experimental Procedure

Before commencing the welding process, the plate's surface oxide layer was removed using an angle grinder and subsequently cleaned with acetone. The activator, previously prepared, was dehumidified using a drying oven and then dissolved in an appropriate amount of acetone solvent. After thorough mixing to form a paste, this paste was manually applied to the cleaned plate surface. TIG welding was carried out using the specified process parameters outlined in Table 2. High-speed cameras were employed to record the arc shape and flow behavior of the weld pool during the welding process. The surface of the weld should be smooth and smooth, without defects such as cracks, biting edges, and welding feet. Metallurgical and mechanical test samples were obtained by utilizing electrical spark line-cutting technology on the acceptable welded plates. The sampling diagram is illustrated in Figure 2. Metallurgical samples underwent grinding, polishing, and etching with aqua regia ( $KCl:HNO_3 = 3:1$ ). The geometric shape and microstructure of the weld were analyzed using an optical microscope (OM).

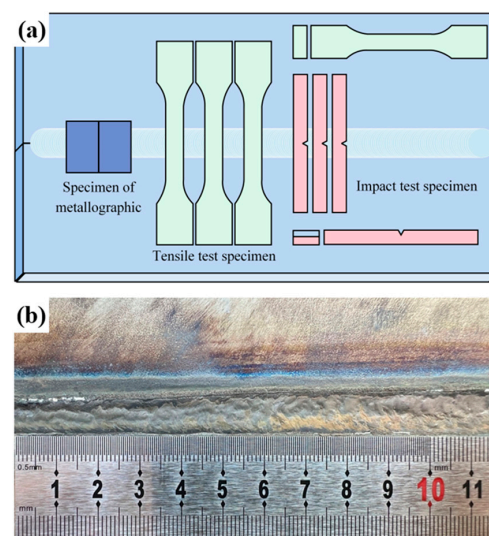


**Figure 2.** Sampling location: (a) Schematic diagram; (b) Profile display.

Microhardness measurements were conducted on the transverse cross-section of the weld sample using a Wilson VH1102 Vickers hardness tester, with the detection locations indicated in Figure 3. The hardness measurement was carried out at a 200 gf load (HV0.2) and a dwell time of 15 s. Tensile tests were using an AGS-X3000 universal testing machine and impact tests were utilizing a Charpy impact-testing machine, with three identical samples prepared to mini-mize errors. The fracture morphology of the tensile and impact samples was observed using an FEG-450 field emission scanning electron microscope (SEM), and element content analysis at specific fracture positions was conducted using the attached energy dispersive spectrometer (EDS).

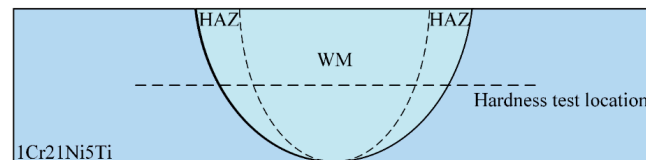


**Figure 3.** Schematic diagram of the microhardness test.

### 3. Results and Discussion

#### 3.1. Effects of the Activated-Flux Type on the Weld Penetration

Figure 4 displays the cross-sections of welding joints for 1Cr21Ni5Ti duplex stainless steel, showcasing the impact of different activated-flux.  $\text{SiO}_2$ ,  $\text{B}_2\text{O}_3$ , and  $\text{Cr}_2\text{O}_3$  activated-flux significantly enhanced weld penetration. Among them,  $\text{Cr}_2\text{O}_3$  yielded the best results, achieving a welding penetration of 5.55 mm and a D/W ratio of 0.60. The corresponding test results are depicted in Figure 5, reinforcing the superior performance of  $\text{Cr}_2\text{O}_3$  as an activated-flux in enhancing weld penetration. Subsequent homogenization tests were conducted on various active agents exhibiting positive effects, and the outcomes are presented in Table 3 and Figure 6. These tests helped determine the optimal active-agent ratio for achieving the desired welding penetration and D/W ratio. The final identified optimal active-agent ratio is discussed below:

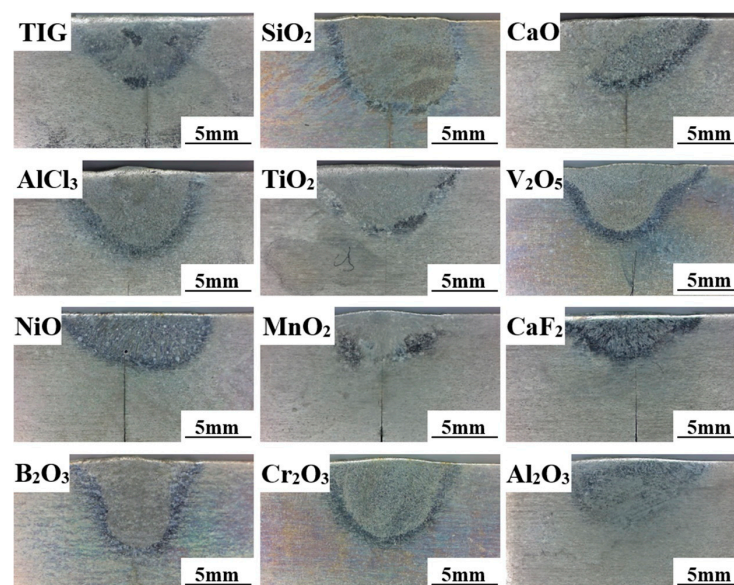


**Figure 4.** Cross-section of the single-component A-TIG welding.

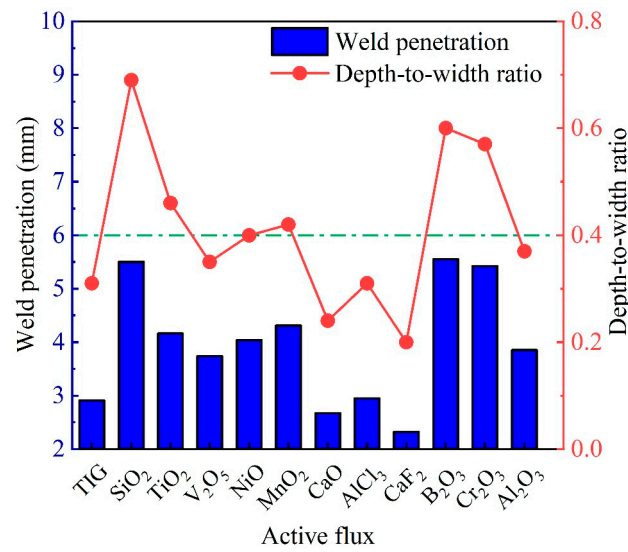


Figure 5. Single-component test results.

Table 3. Uniform design table.

Level	NiO/%	SiO <sub>2</sub> /%	TiO <sub>2</sub> /%	Cr <sub>2</sub> O <sub>3</sub> /%	Al <sub>2</sub> O <sub>3</sub> /%
1	0.548	0.103	0.073	0.057	0.218
2	0.405	0.008	0.319	0.123	0.145
3	0.324	0.188	0.031	0.323	0.133
4	0.265	0.032	0.227	0.456	0.020
5	0.217	0.264	0.413	0.013	0.093
6	0.177	0.062	0.121	0.240	0.400
7	0.142	0.349	0.234	0.172	0.103
8	0.111	0.097	0.017	0.679	0.097
9	0.083	0.459	0.121	0.014	0.324
10	0.057	0.139	0.521	0.083	0.202
11	0.033	0.632	0.037	0.162	0.137
12	0.011	0.183	0.313	0.391	0.103

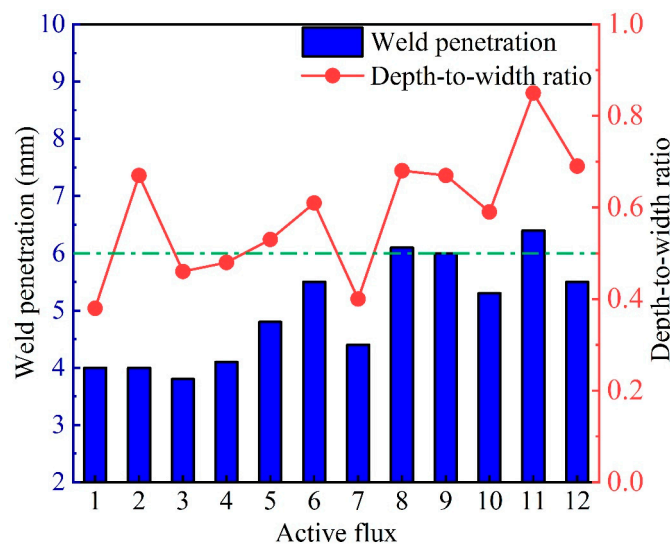
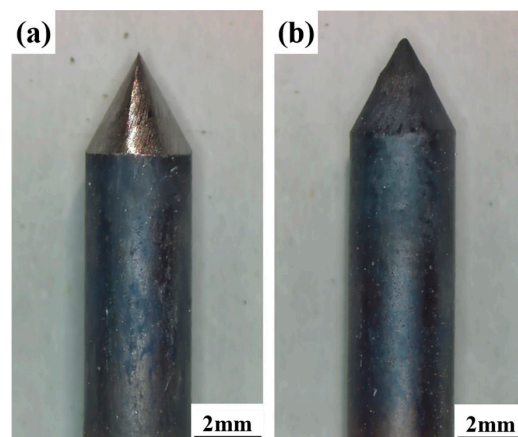


Figure 6. Homogenization test results.

This led to a welding penetration of 6.4 mm, a welding width of 7.5 mm, and  $D/W = 0.85$ . The tensile-strength weld reached 97.5% of the duplex stainless-steel substrate.

In Figure 7a, the morphology of the tungsten electrode prior to A-TIG welding is depicted, while Figure 7b showcases the morphology of the tungsten electrode after A-TIG welding. During the A-TIG welding process, a certain amount of oxygen is generated, causing the tungsten electrode tip to become passive due to the high temperature and oxidation. However, it is important to note that there is no severe damage to the tungsten electrode after welding, as illustrated in Figure 7. The appearance of the tungsten electrode post-A-TIG welding closely resembles that of ordinary TIG welding rods under equivalent welding conditions. This observation strongly suggests that the tungsten electrode is effectively shielded and protected by the shielding gas during the A-TIG welding process. The passivation of the tungsten electrode tip, resulting from oxidation, can influence the performance of the arc plasma. Nevertheless, slight oxidation of the tungsten electrode tip does not have a significant impact on the formation and overall quality of the weld.



**Figure 7.** Tungsten electrode oxidation (a) before welding; (b) after welding.

### 3.2. Comparison of the Welding Formation

Figure 8a,b show the surface and cross-sectional morphology of welds produced under identical conditions using conventional TIG welding and A-TIG welding, respectively. By comparing these, a clear contrast in the weld surface formations and cross-sectional contours between the two welding methods can be observed, as displayed in Figure 8. The weld produced by conventional TIG welding was observed to be broad and shallow. In contrast, A-TIG welding resulted in a narrower yet deeper weld. Remarkably, compared with conventional TIG welding, the weld penetration depth achieved by A-TIG welding increased by a factor of 1.67, as graphically represented in Figure 9.

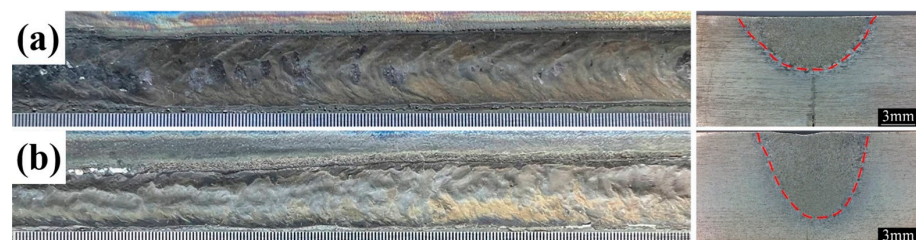


**Figure 8.** Comparison of the welding formation: (a) TIG; (b) A-TIG.

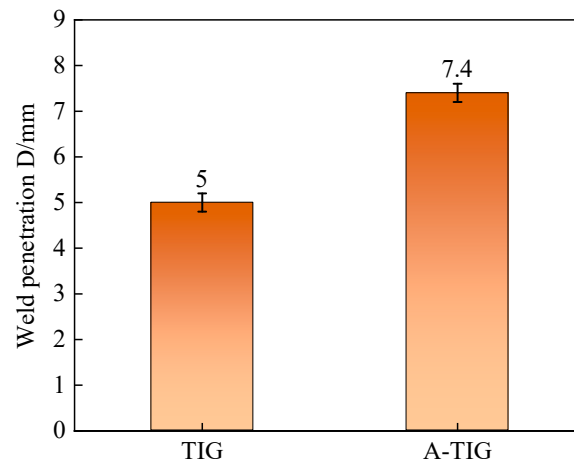


**Figure 9.** Comparison of the weld penetration.

### 3.3. Weld-Shift Experiment

To determine the primary cause of the increased penetration depth, an experimental design involving a weld shift was conceived and executed. This design is illustrated in the schematic diagram presented in Figure 10. The weld-pool flow behavior during A-TIG welding observed by high-speed camera was shown in Figure 11. The figure clearly shows green spots moving from the weld-pool edge to the center. This indirectly proves that with the addition of an active agent, the molten metal moves from the periphery to the center.

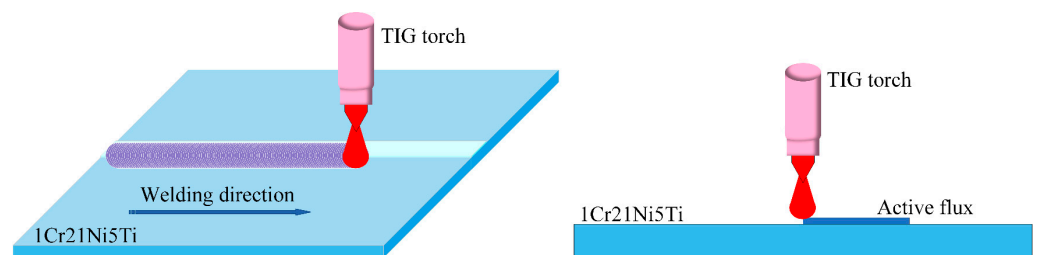


**Figure 10.** Weld-shape experiment diagram.

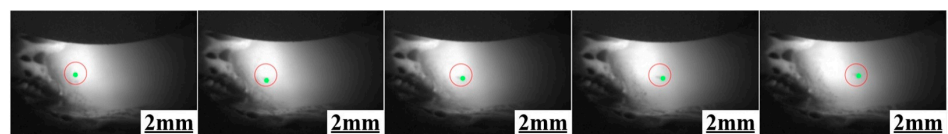


**Figure 11.** Weld-pool flow behavior.

In Figure 12, convection movements within the TIG/A-TIG weld bead are illustrated. During the welding process, an active element is applied to the workpiece's surface being welded. Under the thermal influence of the arc, oxygen atoms continuously accumulate on the molten pool's surface and permeate it. When the diffusion and clustering of oxygen atoms reach an equilibrium, the oxygen element's mass fraction in the molten pool affects the surface-tension gradient coefficient ( $\partial\gamma/\partial T$ ). Due to the presence of oxygen elements, the temperature field range at the molten pool's surface is negative toward the weld center. Except for a small area at the center of the molten pool where the surface-tension temperature gradient coefficient is negative, the edges of the weld pool exhibit a positive gradient. The surface tension near the solid–liquid interface is significantly lower than the surface tension at the weld center, prompting the liquid metal in the molten pool to flow from the periphery to the center, creating two inward vortices—this phenomenon is known as reversed Marangoni convection, as shown in Figure 12. After the reversal of the Marangoni convection, the two vortices converge at the center of the molten pool,

forming an inward vortex that impacts the bottom of the molten pool, effectively bringing more heat to melt the substrate. In a small region at the center of the weld pool, the liquid metal forms a vortex flowing from the center to the periphery of the weld pool due to the negative surface-tension gradient coefficient, propelling the inward vortex forward. The addition of oxygen causes the reversal of the Marangoni convection, elevating the overall temperature of the weld pool, increasing the flow rate of the liquid metal, and resulting in a shift in the depth of the weld penetration.

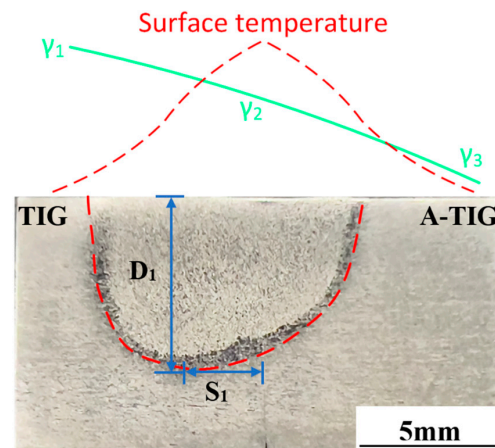


**Figure 12.** Convection movements of the TIG/A-TIG weld bead.

The deepest penetration of the weld in Figure 12 is situated on the left side of the weld joint, tilting toward the TIG welding of the weld joint. Comparatively, the pool surface of TIG welding is higher than that of the 1Cr21Ni5Ti surface and the A-TIG welding pool surface. The approximate measurement locations for the maximum penetration depth ( $D_1 \approx 6.84$  mm) and the center-line shift ( $S_1 \approx 3.21$  mm) position are indicated in Figure 12. By comparing the current findings with the results of previous GTA welding operations [27], it is evident that Marangoni convection flows from the edge of the molten pool toward the center of the weld. Additionally, the increase in oxygen content reduces the surface tension of the steel, ultimately causing the reversal of the Marangoni convection.

In Figure 13, the surface formation of the weld seam from the weld-seam displacement experiment is depicted. Once welding commences, a noticeable undercut-like feature appears on one side of the TIG weld along the weld seam. This feature is characterized by the molten liquid metal receding and solidifying in place, creating a recessed area in the weld. A similar phenomenon is observed at the end of the weld seam. Remarkably, this experimental result aligns with findings documented in the literature, as referenced in [18,28]. The presence of such undercutting is a consistent and anticipated aspect of the welding process, based on the existing body of research.

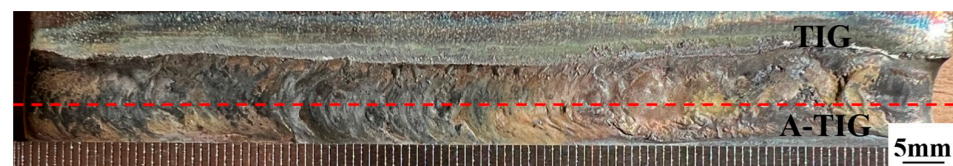


**Figure 13.** Cross-section of the weld profile.

### 3.4. Microstructure and Mechanical Properties

Figure 14a,b show the metallographic structure at the center of a conventional TIG welding joint. Figure 14c,d show the metallographic structure at the center of the A-TIG welding joints. It is obvious that the microstructure of the weld is mainly composed of skeletal ferrite and austenite columnar crystals that grow toward the center of the weld pool along the heat dissipation direction. Under conventional TIG welding, the higher

heat input results in a slower cooling rate, resulting in larger weld grains, as shown in Figure 14a,b. Compared with conventional TIG welding, the grain size at the center of the A-TIG welding seam is relatively smaller. Under A-TIG welding, the addition of oxygen causes a change in surface tension, which results in a reversal of the Marangoni convection, so the thermal cycle, temperature gradient, and cooling rate at different positions of the weld are completely different. Generally speaking, the weld microstructure was not obvious changed.

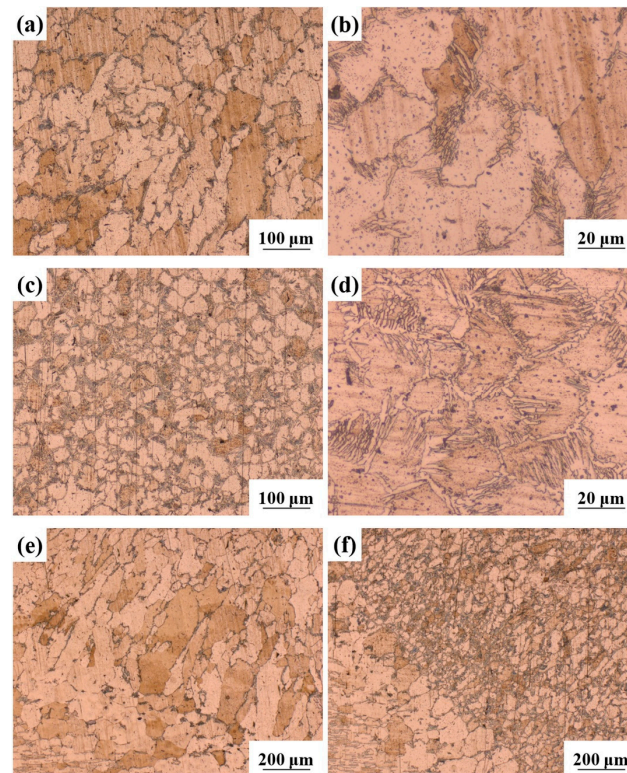


**Figure 14.** Weld microstructures at the (a,b) TIG weld center; (c,d) A-TIG weld center; (e) TIG weld fusion line; and (f) A-TIG weld fusion line.

Figure 14e,f show the microstructure of the heat-affected zone (HAZ) of weld joints. Compared with the weld center, the temperature gradient in the weld heat-affected zone is large, so the metallographic structure is mainly columnar crystals growing perpendicular to the fusion line. The length of the heat-affected zone from TIG welding is 820  $\mu\text{m}$ , and the length of the heat-affected zone upon A-TIG welding is 500  $\mu\text{m}$ . The heat generated by the A-TIG welding arc mainly affects the center of the weld. Due to the heat-affected zone of the weld cooling faster, the heat-affected zone from A-TIG welding is smaller than that from conventional TIG welding.

The solidification mode of 1Cr21Ni5Ti duplex stainless steel's weld pool was determined by considering the ratio of  $[\text{Cr}]_{\text{eq}}/[\text{Ni}]_{\text{eq}}$  by utilizing the Schaeffler formula [29], where  $[\text{Cr}]_{\text{eq}}$  and  $[\text{Ni}]_{\text{eq}}$  represent respectively chromium and nickel equivalents, as illustrated in Equations (1) and (2).

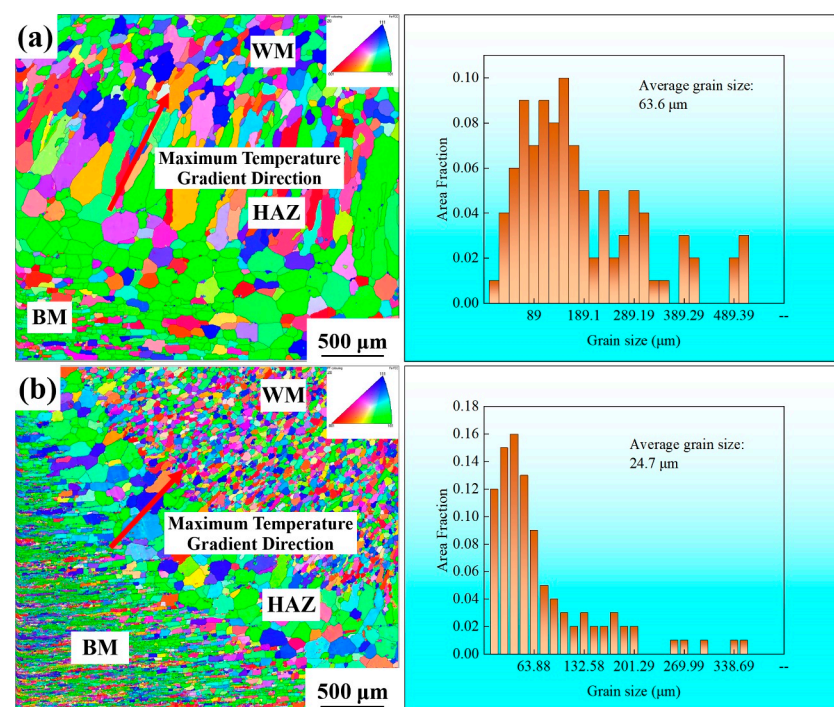
After the welding process, the microstructure of the weld closely resembles that of the 1Cr21Ni5Ti duplex stainless-steel substrate, suggesting a strong alignment. It is hypothesized that the chemical composition of the weld metal mirrors that of the substrate. For precise calculations, we referred to Table 1, which provides the chemical composition of the 1Cr21Ni5Ti duplex stainless steel, enabling us to compute the chromium and nickel equivalents in the weld metal.

$$[\text{Cr}]_{\text{eq}} = W_{\text{Cr}} + W_{\text{MO}} + 1.5W_{\text{Si}} + W_{\text{Nb}} + 2W_{\text{Ti}} \quad (1)$$

$$[\text{Ni}]_{\text{eq}} = W_{\text{Ni}} + 0.5W_{\text{Mn}} + 30W_{\text{C}} \quad (2)$$

The results are  $[\text{Cr}]_{\text{eq}} = 0.22$ ,  $[\text{Ni}]_{\text{eq}} = 0.09$ ,  $[\text{Cr}]_{\text{eq}}/[\text{Ni}]_{\text{eq}} = 2.44$ , the weld solidified in dual ferritic-austenitic (FA) phase mode [30,31]. Duplex stainless steel at high temperature is composed entirely of  $\delta$ -ferrite, and for the solid-state transformation into  $\gamma$ -austenite, alloying elements need to be added to this process to promote and stabilize the formation of the  $\gamma$ -austenite phase. During the cooling process of the weld, the liquid phase forms  $\delta$ -ferrite and gradually grows, and then the peritectic transformation occurs in the  $\delta$ -ferrite structure, and the  $\gamma$ -austenite grains are gradually precipitated to form  $\gamma$ -austenite. Finally, a biphasic structure of  $\delta$ -ferrite and  $\gamma$ -austenite is formed. The  $\delta$ -ferrite is in a skeleton shape and the  $\gamma$ -austenite is lamellar.

The size and orientation of the grain are key to improving the mechanical properties of A-TIG-welded joints [32–34]. Further investigation into the microstructure of A-TIG-welded duplex stainless steel was conducted by using EBSD technology, as depicted in Figure 15.



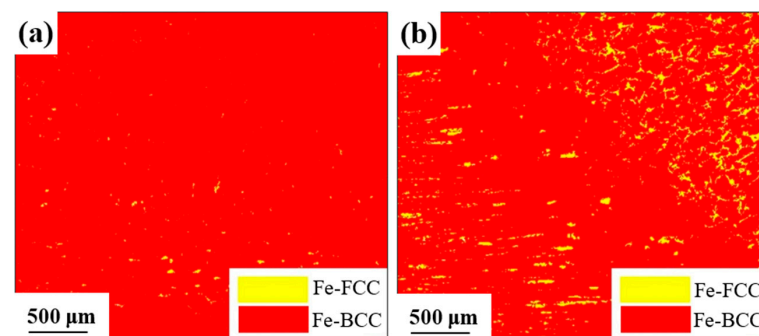
**Figure 15.** Inverse pole and grain size figure in the weld fusion line of (a) TIG and (b) A-TIG samples.

Figure 15a shows the IPF of the fusion-line positions with conventional TIG welding. The IPF of conventional TIG welding indicates that there is an obvious preferred orientation along the maximum temperature gradient, along the  $\langle 101 \rangle$  direction. This experimental result is consistent with the literature mentioned in [35], in which the vertical direction of the fusion line is the maximum temperature gradient direction. In addition, the average grain size of conventional TIG welding is about  $63.6 \mu\text{m}$ , and the maximum value is approximately  $509.4 \mu\text{m}$ .

Figure 15b displays the inverse pole figures and grain distribution at the fusion-line positions in A-TIG welding. The inverse pole figure (IPF) for A-TIG welding indicates the presence of numerous fine grains oriented along the direction of the maximum temperature gradient. The distribution of the grain orientation is relatively uniform, with a slightly noticeable preferred orientation. This observation aligns with the optical microscopy (OM) images depicted in Figure 14e,f. In the A-TIG welding process, an activated-flux was utilized to facilitate welding. This not only enhanced the welding penetration and grain orientation but also led to grain-size refinement. The primary reason for this improvement lies in the hindrance of dislocation motion [36]. The average grain size in A-TIG welds measures

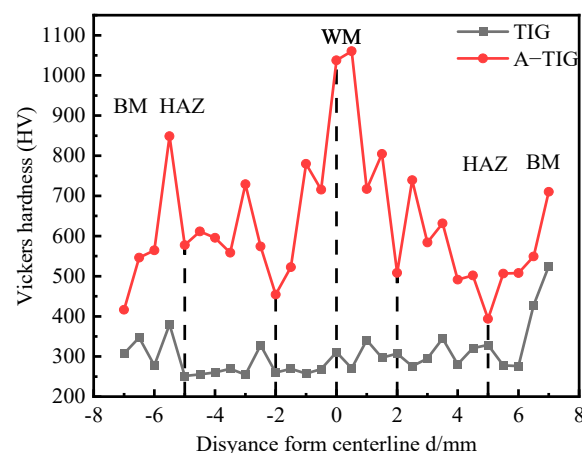
approximately 24.7  $\mu\text{m}$ , with the maximum value exceeding 352.4  $\mu\text{m}$ . When compared with conventional TIG welding joints, A-TIG welding results in welds with complete penetration and a more disordered grain orientation. In summary, the introduction of oxygen, facilitated by the activated-flux, plays a crucial role in restraining weld grain growth and impeding dislocation motion within the weld. Consequently, this process leads to grain-size reduction.

Figure 16 shows the phase diagrams of the conventional TIG-welded joint and the A-TIG-welded joint. Figure 16a displays the FCC structure and BCC structure in the TIG-welded joint; the austenite (FCC) is represented by yellow, and the ferrite (BCC) is represented by red. This result directly demonstrates that the cooling process of a duplex stainless-steel weld leads to the formation of austenite and ferrite in the microstructure of the weld. The volume fraction of ferrite is relatively small, only 0.006, and it is primarily distributed at the boundaries of the austenite. Figure 16b displays the FCC structure and BCC structure in the A-TIG-welded joint. Compared with conventional TIG welding, the volume fraction of ferrite in the microstructure of the A-TIG weld is over 0.069, significantly higher than that in conventional TIG welding. The most critical observation is that the ferrite content in A-TIG welding increased by 91.3% compared with conventional TIG welding. This could be due to factors such as the cooling rate, metallurgical environment, and heat input in the A-TIG-welded joint cooling process.



**Figure 16.** Phase figure in the fusion line of samples: (a) TIG; (b) A-TIG.

Figure 17 shows the microhardness distribution of welded joints. The distribution is almost symmetrical, with A-TIG welding having an overall higher microhardness than conventional TIG welding. The addition of oxygen also resulted in the formation of oxide particles in the weld, thereby increasing the overall hardness of the weld.



**Figure 17.** Microhardness distribution between conventional TIG welding and A-TIG welding.

In Figure 18, the fracture morphology of 1Cr21Ni5Ti, conventional TIG welding, and A-TIG-welded joints during tensile testing is presented, with fractures observed in the heat-

affected zone. Figure 19 illustrates the tensile-test results. In all three tensile specimens, the fractures occur in the base metal (BM), and they exhibit plastic deformation characteristics.

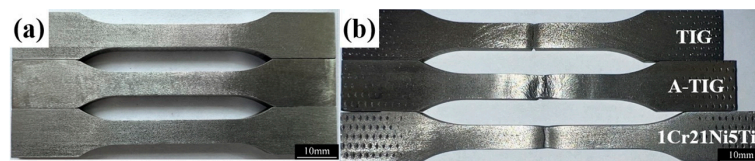


**Figure 18.** Tensile-fracture macroscopic morphology of the welded joint (a) before and (b) after welding.

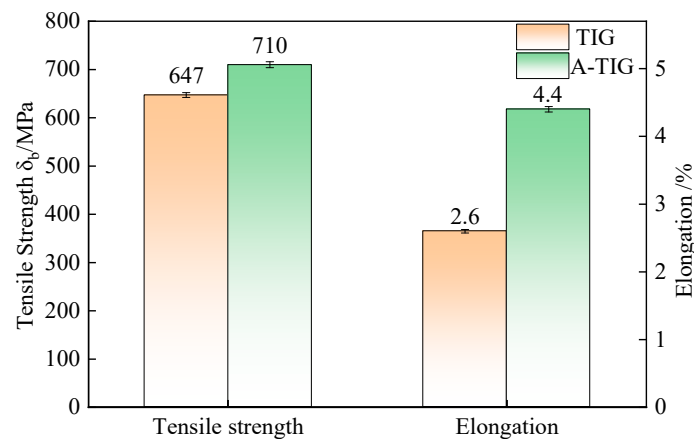


**Figure 19.** Tensile-test result.

The 1Cr21Ni5Ti duplex stainless steel possesses superplastic properties. Under tensile forces, the metal crystal lattice undergoes elastic distortion, resulting in elastic deformation, and the stress–strain relationship demonstrates stable growth. Beyond the plastic limit, some crystals start to slide along specific crystal faces and directions, leading to plastic deformation. At this point, the weld enters the strengthening stage, with stress steadily increasing until it reaches a yield point, and the deformation of the material rapidly increases. Plastic deformation then occurs at the weakest point of the test, reducing the force-bearing area, subsequently causing a gradual decrease in tensile stress, initiating necking until fracture. The tensile properties of the A-TIG welded joint exhibit good performance, with a tensile strength slightly lower than that of the substrate. Conversely, the conventional TIG-welded joint displays poor tensile properties.

Figure 20a,b show the tensile-fracture morphology of the tensile test. Figure 20c,d show the tensile-fracture morphology of 1Cr21Ni5Ti. Figure 20e,f show the tensile-fracture morphology of conventional TIG-welded joints. Figure 20g,h show the tensile-fracture morphology of A-TIG-welded joints. After necking, the metal suddenly breaks, and the tensile fracture is flush, which results in a brittle fracture. Fracture surfaces were observed by SEM. Shear-lip areas exhibit oval-shaped dimples and other areas display circular dimples of varying sizes, which correspond to the characteristics of a plastic fracture and indicate well toughness of the well, as shown in Figure 20. Compared with the microstructure of conventional TIG welding joints, the A-TIG welding joint has a more delicate and even distribution of dimples. Large dimples are surrounded by smaller dimples and tearing ridges. The main reason for this is that the weld contains a significant amount of equiaxed grains, as shown in Figure 14c. The equiaxed structure in the weld is isotropic, whereas the columnar structure is anisotropic. The presence of the equiaxed structure in the weld enhances the isotropy of the weld. The tensile strength of A-TIG welding is higher than that of conventional TIG welding because there is a certain amount of equiaxed grains in the weld.

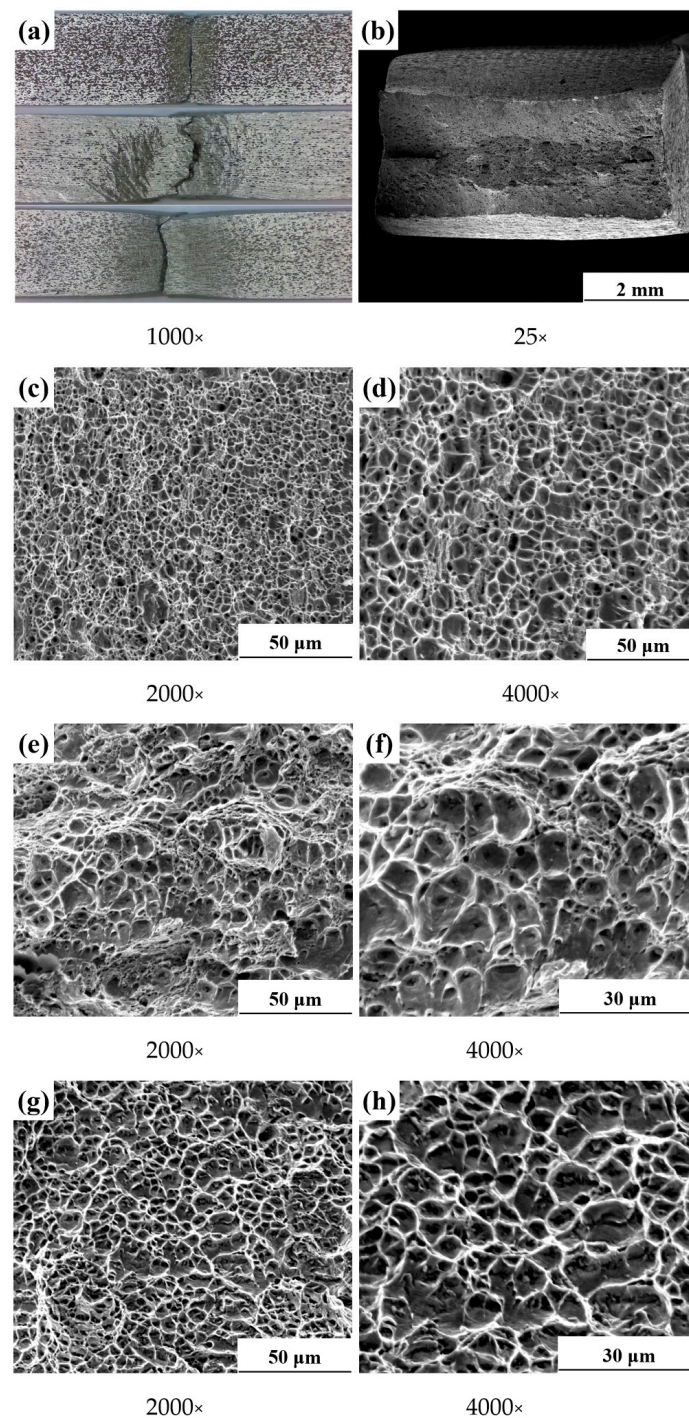


**Figure 20.** Tensile-fracture morphology: (a–d) 1Cr21Ni5Ti; (e,f) TIG; (g,h) A-TIG.

Upon further analysis of the A-TIG-welded joint tensile-fracture morphology, some weld particles appeared in the dimples. SEM for element content analysis reveals that these weld particles are oxides formed by the addition of oxygen to the weld, as shown in Figure 21 and Table 4. These weld particles create slag inclusions, which cause the tensile strength to decrease, impede the movement of the dislocation in the weld, increase the plasticity of the weld, and reduce the toughness of weld, ultimately resulting in an A-TIG-welded joint tensile strength lower than that of a 1Cr21Ni5Ti duplex stainless-steel substrate. Generally speaking, the oxygen content in A-TIG welding is moderate and has little impact on the mechanical properties of the weld.

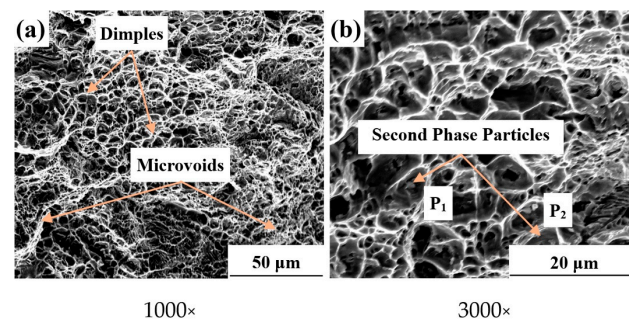


Figure 21. Fracture morphology of the tensile test.

Table 4. EDS test results of the  $P_1$  and  $P_2$  elements as shown in Figure 21b (wt.%).

Elements	O	Fe	Cr	Ni	Ti	Si
$P_1$	40.3	41.4	14.7	2.7	0.6	0.3
$P_2$	35.2	49.9	11.8	2.1	0.6	0.4

Figure 22 shows the macroscopic appearance of the fracture surface from an impact test, and Figure 23 lists the impact energy ( $A_K$ ) for conventional TIG and A-TIG welds. The impact energy ( $A_K$ ) of the A-TIG weld does not differ much from that of the 1Cr21Ni5Ti duplex stainless-steel substrate, which indicates that when the amount of oxygen is mixed, A-TIG can improve the mechanical properties of the weld.

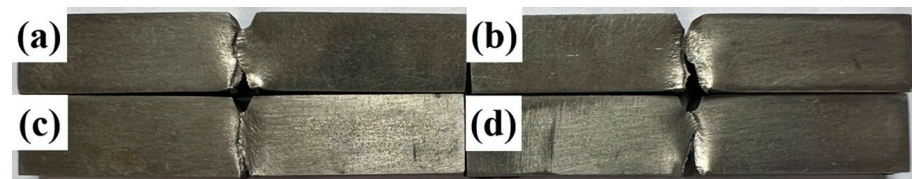


Figure 22. Surface appearance of an impact fracture: (a,b) 1Cr21Ni5Ti; (c) TIG; (d) A-TIG.

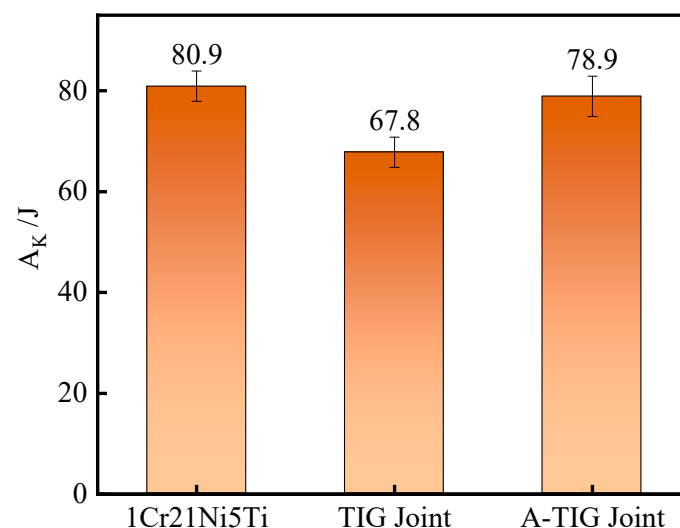
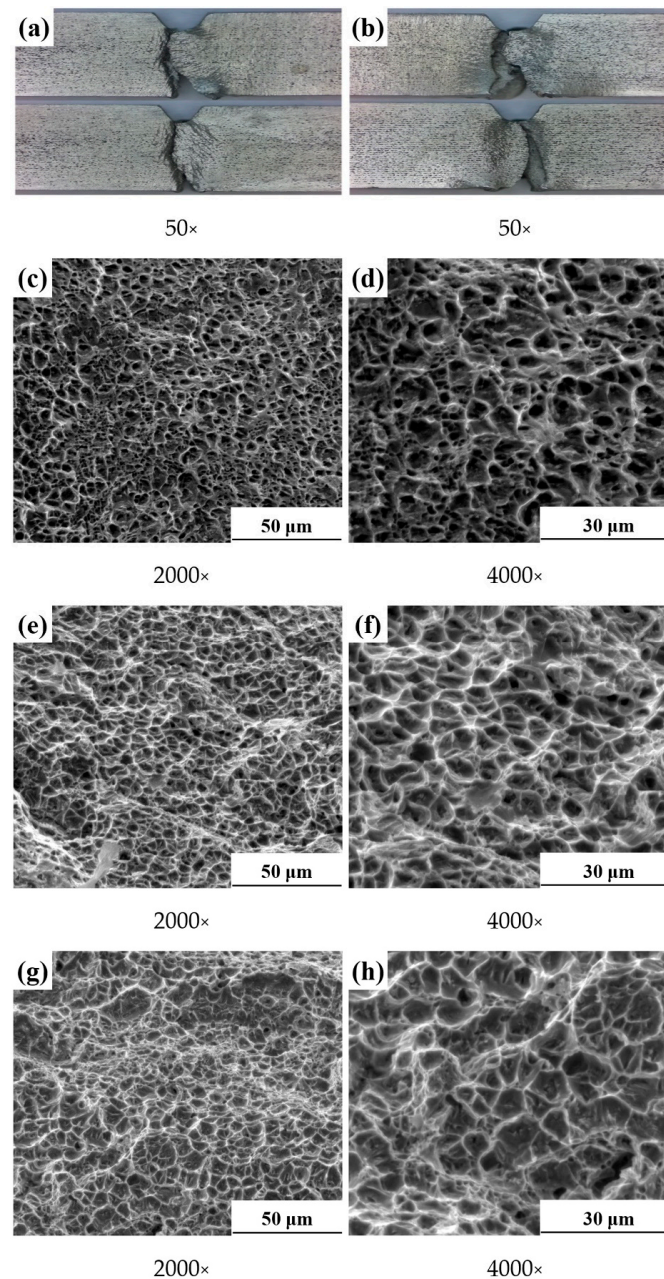


Figure 23. Impact-test result.

Figure 24a,b depict the impact-fracture morphology, while Figure 24c,d show the impact-fracture morphology of 1Cr21Ni5Ti. Figure 24e,f present the impact-fracture morphology of conventional TIG-welded joints, and Figure 24g,h showcase the impact-fracture morphology of A-TIG-welded joints. The impact-fracture surface of the weld predomi-

nantly consists of dimples, with larger dimples containing smaller ones. During deformation, second-phase points within the material gradually disengage from the matrix, forming numerous micropores. Under stress, these micropores evolve into microcracks, ultimately leading to a fracture. The final fracture surface exhibits irregular dimples, as depicted in Figure 24. In terms of impact-fracture morphology, A-TIG welding displays finer and more uniform pits compared with conventional TIG welding. Larger dimples are scattered among the smaller ones. The weld exhibits a significant amount of equiaxed grains, as shown in Figure 14c. This equiaxed structure in the weld is isotropic, contrasting with the anisotropic columnar structure. Consequently, A-TIG welding demonstrates greater impact strength compared with conventional TIG welding.



**Figure 24.** Fracture of a welded-joint impact test: (a–d) 1Cr21Ni5Ti; (e,f) TIG; (g,h) A-TIG.

Upon conducting a thorough analysis of the impact-fracture surface of the A-TIG-welded joint, numerous weld particles were observed within the dimples. These particles were larger in volume and possessed a wedge-like shape. They contributed to weld

strengthening by impeding dislocation movement within the weld, consequently increasing hardness while reducing toughness. Elemental analysis confirmed these particles to be oxides, as depicted in Figure 25 and summarized in Table 5. During the welding process, oxygen from the activator was introduced into the weld. Some of this oxygen formed oxide inclusions within the weld, while the rest existed in the form of oxygen atoms within the weld structure. The presence of these weld particles and oxides affected the crystal structure, ultimately leading to lower impact energy in the A-TIG-welded joint compared with the 1Cr21Ni5Ti duplex stainless-steel substrate. In summary, the oxygen content in A-TIG welding is moderate and has a minor impact on the mechanical properties. However, it is important to note that these oxides and weld particles contribute to weld strengthening and increased hardness at the cost of reduced toughness.

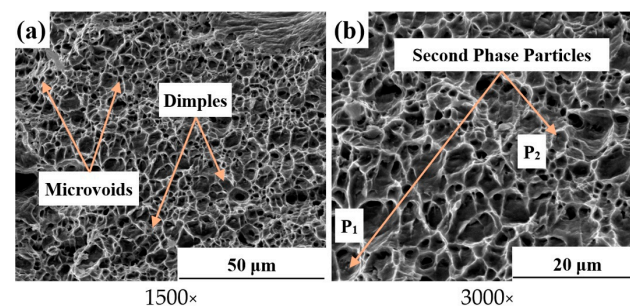


**Figure 25.** Fracture morphology of the impact test.

**Table 5.** EDS test results of the P<sub>1</sub> and P<sub>2</sub> elements as shown in Figure 25b (wt.%).

Elements	O	Fe	Cr	Ni	Ti	Si
P <sub>1</sub>	42.8	39.2	14.3	2.7	0.6	0.4
P <sub>2</sub>	49.5	33.4	14.6	1.5	0.8	0.2

#### 4. Conclusions

Based on the above results and discussion, the influence of different activated-flux and welding process parameters on weld surface formation, microstructure, and mechanical properties was studied, and the mechanism of A-TIG weld-shape improvement and penetration increase in stainless steel was analyzed. Finally, the main results are as follow:

1. In the A-TIG welding process of 1Cr21Ni5Ti stainless steel, the primary factor contributing to the increased penetration depth was the reversal of Marangoni convection. When employing the optimal activator ratio (0.033NiO + 0.632SiO<sub>2</sub> + 0.037TiO<sub>2</sub> + 0.162Cr<sub>2</sub>O<sub>3</sub> + 0.137Al<sub>2</sub>O<sub>3</sub>) and optimal welding parameters (current I = 245A, speed V = 80 mm/min), A-TIG welding achieved a 1.67-fold increase in weld penetration depth compared with conventional TIG welding.
2. In terms of microstructure, A-TIG welding led to a significant improvement. It reduced the overall grain size within the weld by 61.2%, with the maximum grain-size shrinking by 30.8%, leading to a more disordered grain orientation. Furthermore, the ferrite content showed a remarkable increase of 91.3%.
3. In contrast to conventional TIG welding, A-TIG-welded joints demonstrate notable improvements in several aspects. These include a higher overall hardness, an increased tensile strength of 10.3%, a substantial elongation increase of 69.2%, and a noticeable enhancement in impact energy of 16.3%.

**Author Contributions:** Conceptualization, Y.H. and X.Y.; Methodology, S.Y.; Software, Y.H.; Validation, Y.H. and Y.N.; Formal analysis, X.Y.; Investigation, J.Z.; Resources, Y.N.; Data curation, Y.N.; Writing—original draft, S.Y.; Writing—review & editing, S.Y.; Project administration, D.F.; Funding acquisition, D.F. All authors have read and agreed to the published version of the manuscript.

**Funding:** This research was funded by National Natural Science Foundation grant number 51965036.

**Data Availability Statement:** All data generated or analyzed during this study are included in this published article. The experimental data in this article can be used for scientific research, teaching, etc.

**Conflicts of Interest:** The authors declare that they have no competing financial interest or personal relationships that may have influenced the work reported in this study.

## References

1. Rodrigues, D.G.; Maria, G.G.B.; Viana, N.A.L.; Santos, D.B. Effect of low cold-rolling strain on microstructure, texture, phase transformation, and mechanical properties of 2304 lean duplex stainless steel. *Mater. Charact.* **2019**, *150*, 138–149. [[CrossRef](#)]
2. Zhang, X.; Wang, K.; Zhou, Q.; Ding, J.; Ganguly, S.; Marzio, G.; Yang, D.; Xu, X.; Dirisu, P.; Williams, S.W. Microstructure and mechanical properties of TOP-TIG-wire and arc additive manufactured super duplex stainless steel (ER2594). *Mater. Sci. Eng. A* **2019**, *762*, 138097. [[CrossRef](#)]
3. Quackatz, L.; Griesche, A.; Kannengiesser, T. In situ investigation of chemical composition during TIG welding in duplex stainless steels using Laser-Induced Breakdown Spectroscopy (LIBS)-ScienceDirect. *Forces Mech.* **2021**, *6*, 2666–3597. [[CrossRef](#)]
4. Liu, J.; Das, Y.; Babu, R.P.; Wessman, S.; Jonsson, J.Y.; Odqvist, J.; King, S.M.; Hedström, P. Small-angle neutron scattering study on phase separation in a super duplex stainless steel at 300 °C—Comparing hot-rolled and TIG welded material. *Mater. Charact.* **2022**, *190*, 112044. [[CrossRef](#)]
5. Jebaraj, A.V.; Ajaykumar, L.; Deepak, C.; Aditya, K. Weldability, machinability and surfacing of commercial duplex Stainless Steel AISI2205 for marine applications –A recent review. *J. Adv. Res.* **2017**, *8*, 183–199. [[CrossRef](#)] [[PubMed](#)]
6. Zhang, W.W.; Cong, S.; Luo, S.B.; Fang, J.H. Effects of Energy Density and Shielding Medium on Performance of Laser Beam Welding (LBW) Joints on SAF2205 Duplex Stainless Steel. *J. Miner.* **2018**, *70*, 1554–1559. [[CrossRef](#)]
7. Xu, X.; Odqvist, J.; Colliander, M.H.; King, S.; Thuvander, M.; Steuerer, A.; Hedström, P. Effect of cooling rate after solution treatment on subsequent phase separation during aging of Fe-Cr alloys: A small-angle neutron scattering study. *Acta Mater.* **2017**, *134*, 221–229. [[CrossRef](#)]
8. Xu, X.; Westraadt, J.E.; Odqvist, J.; Youngs, T.G.; King, S.M.; Hedström, P. Effect of heat treatment above the miscibility gap on nanostructure formation due to spinodal decomposition in Fe-52.85 at. %Cr. *Acta Mater.* **2018**, *145*, 347–358. [[CrossRef](#)]
9. Hosseini, V.A.; Thuvander, M.; Lindgren, K.; Oliver, J.; Folkesson, N.; Gonzalez, D.; Karlsson, L. Fe and Cr phase separation in super and hyper duplex stainless steel plates and welds after very short aging times. *Mater. Des.* **2021**, *210*, 110055. [[CrossRef](#)]
10. Ouali, N.; Khenfer, K.; Belkessa, B.; Fajoui, J.; Cheniti, B.; Idir, B.; Branchu, S. Effect of Heat Input on Microstructure, Residual Stress, and Corrosion Resistance of UNS 32101 Lean Duplex Stainless Steel Weld Joints. *J. Mater. Eng. Perform.* **2019**, *28*, 4252–4264. [[CrossRef](#)]
11. Tian, H.; Cheng, X.; Wang, Y.; Dong, C.; Li, X. Effect of Mo on interaction between alpha/gamma phases of duplex stainless steel. *Electrochim. Acta* **2018**, *267*, 255–268. [[CrossRef](#)]
12. Zhou, J.; Odqvist, J.; Ruban, A.; Thuvander, M.; Xiong, W.; Ågren, J.; Olson, G.B.; Hedström, P. Effect of solution treatment on spinodal decomposition during aging of an Fe-46.5 at.% Cr alloy. *J. Mater. Sci.* **2017**, *52*, 326–335. [[CrossRef](#)]
13. Hosseini, V.A.; Lindgren, K.; Thuvander, M.; Gonzalez, D.; Oliver, J.; Karlsson, L. Nanoscale phase separations in as-fabricated thick super duplex stainless steels. *Mater. Sci. Technol.* **2021**, *56*, 12475–12485. [[CrossRef](#)]
14. Keplinger, A.; Martinez, C.; Hausbauer, M.; Kapp, M. Early Stages of Deleterious Phases in Super and Hyper Duplex Stainless Steel and Their Effect on Toughness. *Berg Huettenmaenn Monatsh* **2020**, *165*, 33–39. [[CrossRef](#)]
15. Hosseini, V.A.; Hurtig, K.; Karlsson, L. Effect of multipass TIG welding on the corrosion resistance and microstructure of a super duplex stainless steel. *Mater. Corros.* **2017**, *68*, 405–415. [[CrossRef](#)]
16. Dhandha, K.H.; Badheka, V.J. Effect of activating fluxes on weld bead morphology of P91 steel bead-on-plate welds by flux assisted tungsten inert gas welding process. *J. Manuf. Process.* **2015**, *17*, 48–57. [[CrossRef](#)]
17. Cai, Y.; Luo, Z.; Huang, Z.; Zeng, Y. Effect of cerium oxide flux on active flux TIG welding of 800 MPa super steel. *J. Mater. Process. Technol.* **2016**, *230*, 80–87. [[CrossRef](#)]
18. Anup, K.; Dwivedi, D.K.; Vasudevan, M. Study of mechanism, microstructure and mechanical properties of activated flux TIG welded P91 Steel-P22 steel dissimilar metal joint. *Mater. Sci. Eng. A* **2018**, *731*, 309–323. [[CrossRef](#)]
19. Pinheiro, F.W.; de Souza, L.M.; Pereira, E.C.; Monteiro, S.N.; Azevedo, A.R. Effect of solubilization heat treatment on microstructure and corrosion resistance of joints welded with the autogenous TIG process duplex stainless steel. *J. Mater. Res. Technol.* **2023**, *26*, 1527–1536. [[CrossRef](#)]
20. Wang, B.; Christiansen, T.L.; Somers, M.A. Influence of ferrite-austenite distribution in 2205 duplex stainless steel on high-temperature solution nitriding behaviour. *Surf. Coat. Technol.* **2023**, *453*, 129134. [[CrossRef](#)]
21. Zhang, Z.; Jing, H.; Xu, L.; Han, Y.; Zhao, L.; Lv, X.; Zhang, J. The impact of annealing temperature on improving microstructure and toughness of electron beam welded duplex stainless steel. *J. Manuf. Process.* **2018**, *31*, 568–582. [[CrossRef](#)]
22. Xu, Y.; Dong, Z.; Wei, Y.; Yang, C. Marangoni convection and weld shape variation in A-TIG welding process. *Theor. Appl. Fract. Mech.* **2007**, *48*, 178–186. [[CrossRef](#)]
23. Wang, X.; Huang, J.; Huang, Y.; Fan, D.; Guo, Y. Investigation of heat transfer and fluid flow in activating TIG welding by numerical modeling. *Appl. Therm. Eng. Des. Process. Equip. Econ.* **2017**, *113*, 27–35. [[CrossRef](#)]

24. Aucott, L.; Dong, H.B.; Mirihanage, W.; Atwood, R.; Kidess, A.; Gao, S.A.; Wen, S.W.; Marsden, J.; Feng, S.; Tong, M.M.; et al. Revealing internal flow behavior in arc welding and additive manufacturing of metals. *Nat. Commun.* **2018**, *9*, 5414. [[CrossRef](#)]
25. Modenesi, P.J.; Neto, P.C.; Apolinário, E.R.; Dias, K.B. Effect of flux density and the presence of additives in ATIG welding of austenitic stainless steel. *Weld. Int.* **2015**, *29*, 425–432. [[CrossRef](#)]
26. Liu, G.-H.; Liu, M.-H.; Yi, Y.-Y.; Zhang, Y.-P.; Luo, Z.-Y.; Xu, L. Activated flux tungsten inert gas welding of 8mm-thick AISI 304 austenitic stainless steel. *J. Cent. South Univ.* **2015**, *22*, 800–805. [[CrossRef](#)]
27. Lippold, J.C.; Savage, W.F. Solidification of austenitic stainless steel weldments: Part 2-The effect of alloy composition on ferrite morphology. *Weld. J.* **1980**, *59*, 48–58.
28. Vidyarthi, R.S.; Kulkarni, A.; Dwivedi, D.K. Study of microstructure and mechanical property relationships of A-TIG welded P91–316L dissimilar steel joint. *Mater. Sci. Eng. A* **2017**, *695*, 249–257. [[CrossRef](#)]
29. Nayee, S.G.; Badheka, V.J. Effect of oxide-based fluxes on mechanical and metallurgical properties of dissimilar activating flux assisted-tungsten inert gas welds. *J. Manuf. Process.* **2014**, *16*, 137–143. [[CrossRef](#)]
30. Saeid, T.; Abdollah-Zadeh, A.; Assadi, H.; Ghaini, F.M. Effect of friction stir welding speed on the microstructure and mechanical properties of a duplex stainless steel. *Mater. Sci. Eng. A* **2008**, *496*, 262–268. [[CrossRef](#)]
31. Verma, J.; Taiwade, R.V.; Kataria, R.; Kumar, A. Welding and electrochemical behavior of ferritic AISI 430 and austeno-ferritic UNS 32205 dissimilar welds. *J. Manuf. Process.* **2018**, *34*, 292–302. [[CrossRef](#)]
32. Tokita, S.; Kokawa, H.; Sato, Y.S.; Fujii, H.T. In situ EBSD observation of grain boundary character distribution evolution during thermo mechanical process used for grain boundary engineering of 304 austenitic stainless steel. *Mater. Charact.* **2017**, *131*, 31–38. [[CrossRef](#)]
33. Zhang, Z.; Jing, H.; Xu, L.; Han, Y.; Zhao, L. Investigation on microstructure evolution and properties of duplex stainless steel joint multi-pass welded by using different methods. *Mater. Des.* **2016**, *109*, 670–685. [[CrossRef](#)]
34. Zhang, J.; Shao, P.; Wang, X.; Fan, D. Improving weld penetration by two-TIG arc activated via mixing oxygen into shielding gas. *Int. J. Adv. Manuf. Technol.* **2023**, *125*, 169–181. [[CrossRef](#)]
35. Lienert, T.; Burgardt, P.; Harada, K.; Forsyth, R.; DebRoy, T. Weld bead center line shift during laser welding of austenitic stainless steels with different sulfur content. *Scr. Mater.* **2014**, *71*, 37–40. [[CrossRef](#)]
36. Wang, L.; Xue, J.; Wang, Q. Correlation between arc mode, microstructure, and mechanical properties during wire arc additive manufacturing of 316L stainless steel. *Mater. Sci. Eng. A* **2019**, *751*, 183–190. [[CrossRef](#)]

**Disclaimer/Publisher’s Note:** The statements, opinions and data contained in all publications are solely those of the individual author(s) and contributor(s) and not of MDPI and/or the editor(s). MDPI and/or the editor(s) disclaim responsibility for any injury to people or property resulting from any ideas, methods, instructions or products referred to in the content.